Energy & Environmental Science

ROYAL SOCIETY OF CHEMISTRY

PAPER

View Article Online
View Journal | View Issue

Check for updates

Cite this: *Energy Environ. Sci.*, 2024, **17**, 1141

Realizing horizontal magnesium platelet deposition and suppressed surface passivation for high-performance magnesium metal batteries†

Gaoliang Yang,[a] Yuanjian Li,[a] Jianbiao Wang,[a] Yanwei Lum,[a] Carina Yi Jing Lim,[a] Man-Fai Ng,[b] Chang Zhang,[c] Zhi Chang,[d] Zhonghan Zhang,[e] Albertus D. Handoko,[a] Tanmay Ghosh,[a] Shuzhou Li,[e] Zdenek Sofer,[f] Wei Liu,[c] Yan Yao*[gh] and Zhi Wei Seh*[a]

Received 17th July 2023,
Accepted 5th December 2023

DOI: 10.1039/d3ee02317f

rsc.li/ees

Rechargeable magnesium batteries (RMBs) are emerging as promising alternatives to lithium-ion batteries due to their high volumetric capacity and natural abundance. However, challenges arising from severe passivation and uneven deposition in conventional electrolytes persist, resulting in poor reversibility and cycling stability. Herein, a covalent molecule of 1-chloropropane (CP) is introduced into conventional electrolytes to manipulate the kinetics and surface chemistry of Mg anodes. Stemming from the reduced surface energy of the Mg (002) crystal plane from CP–Mg interactions, a horizontally arranged platelet morphology with enhanced (002) orientations is preferentially formed during the electrodeposition process. Moreover, the appropriate lowest unoccupied molecular orbital energy level of CP enables a robust Cl-rich interphase *in situ* formed on the Mg electrode surface. The planar deposition morphology coupled with the protective interphase can effectively suppress parasitic reactions between Mg electrodes and electrolytes and facilitate the electrochemical reaction kinetics. The as-designed electrolyte achieves reversible Mg plating/stripping with a high coulombic efficiency of 99.79% in asymmetric cells and maintains stable cycling for over 215 h in symmetric cells at an ultrahigh current density of 25 mA cm^{-2}, outperforming previously reported results. This engineered electrolyte also exhibits excellent compatibility with different inorganic/organic cathode materials, offering promising opportunities for RMB applications.

Broader context

Magnesium (Mg) metal batteries have attracted extensive attention due to their high theoretical volumetric capacity and natural abundance, but still suffer from poor reversibility and cycling stability due to sluggish kinetics and inevitable side reactions. Most of the existing studies mainly focus on improving the reversibility of Mg plating/stripping, while few explorations have been conducted on regulating the Mg deposition behaviors, which may lead to detrimental loss of active materials and pose as a safety hazard under certain conditions. Herein, we demonstrate a covalent molecule of 1-chloropropane for manipulating the kinetics and surface chemistry of Mg anodes in conventional electrolytes, realizing horizontally arranged Mg platelet electrodeposition with preferential orientations of the (002) crystal plane and *in situ* formation of the Cl-rich interphase on Mg electrode surface. The as-designed electrolyte achieves remarkable cycling performance under working conditions suitable for commercial adoption (5 mA cm^{-2}/5 mA h cm^{-2}) as well as the ultra-high current density of 25 mA cm^{-2}. Our work highlights the importance of surface/interface modulation *via* electrolyte modification to inhibit surface passivation and realize planar Mg deposition, and provides new insights for regulating the Mg deposition behaviors through correlating crystallography and morphology for the development of high-performance Mg metal batteries.

[a] *Institute of Materials Research and Engineering (IMRE), Agency for Science, Technology and Research (A*STAR), 2 Fusionopolis Way, Innovis #08-03, Singapore 138634, Republic of Singapore. E-mail: sehzw@imre.a-star.edu.sg*
[b] *Institute of High Performance Computing (IHPC), Agency for Science, Technology and Research (A*STAR), 1 Fusionopolis Way, #16-16 Connexis, Singapore 138632, Republic of Singapore*
[c] *School of Physical Science and Technology, ShanghaiTech University, Shanghai 201210, China*
[d] *Department of Materials Physics and Chemistry, School of Materials Science & Engineering, Central South University, Changsha, 410083, Hunan, China*
[e] *School of Materials Science and Engineering, Nanyang Technological University, 50 Nanyang Ave, Singapore 639798, Republic of Singapore*
[f] *Department of Inorganic Chemistry, University of Chemistry and Technology Prague, Technická 5, 166 28 Prague 6, Czech Republic*
[g] *Department of Electrical and Computer Engineering, University of Houston, Houston, TX 77204, USA. E-mail: yyao4@central.uh.edu*
[h] *Texas Center for Superconductivity at the University of Houston (TcSUH), University of Houston, Houston, TX 77204, USA*

† Electronic supplementary information (ESI) available: Experimental and computational details, supplementary figures, and supplementary tables. See DOI: https://doi.org/10.1039/d3ee02317f

Introduction

The increasing demands of energy storage solutions warrant a pressing need for next-generation battery systems beyond conventional lithium-ion batteries (LIBs).[1–3] Due to their high theoretical volumetric capacity (3833 mA h cm^{-3}) and the earth-abundance of magnesium (Mg) metal, rechargeable magnesium batteries (RMBs) are considered as one of the most promising post-LIB technologies.[4–6] However, given the intrinsically low reduction potential of Mg metal (−2.37 V *versus* a standard hydrogen electrode), Mg anodes are susceptible to reactions with most electrolyte components, forming a solid film on the surface.[7,8] This kind of film typically passivates the Mg anode and impedes reversible Mg plating/stripping due to the sluggish diffusion kinetics of Mg^{2+} through this interphase.[9,10] Therefore, constructing a Mg^{2+}-conducting interphase on Mg anodes to inhibit the surface passivation is crucial for achieving efficient Mg batteries.[11] Recently, a myriad of artificial protective layers for Mg anodes have been studied, including metal/alloys,[12,13] magnesium halides,[14,15] and organic polymers.[16,17] Although such decorated artificial layers facilitated ionic diffusion and reversible cycling in conventional electrolytes, drawbacks include possible damage and detachment of these layers from the Mg electrodes due to the volume or structure changes during continuous plating/stripping, resulting in increased voltage hysteresis during prolonged cycles.[18,19] Therefore, building a robust interphase layer on Mg electrodes *via* the *in situ* (electro-)chemical reactions within the system – that is both permeable to Mg^{2+} whilst simultaneously protecting the Mg electrode from detrimental side reactions – is highly desirable for stabilizing the Mg anode during long-term cycling.[20–22]

Even though *in situ* formed interphases can relieve the surface passivation on Mg anodes, the propensity of Mg to form rough, nonuniform electrodeposits is another critical barrier against developing efficient Mg batteries.[19,23] These electrodeposits lead to detrimental loss of active materials and pose as a safety hazard, given their potential to trigger short circuits under certain conditions.[8,24,25] Hence, gaining a better understanding of the key factors influencing Mg deposition and developing strategies to modulate them are vital for the practical implementation of RMBs. One of the governing factors for Mg deposition morphology is the energy barrier during the nucleation and crystallization processes, where the system must overcome the energy barrier associated with the surface energy increment due to the creation of new interfaces.[26,27] Therefore, controlling the surface energy for different crystal planes may promote the preferential formation of Mg grains with a specific morphology.[28,29] As a hexagonal close-packed (hcp) metal, the basal plane of Mg (002) possesses the lowest surface energy and highest packing density compared with other crystal planes.[27,30,31] Consequently, during electrodeposition, the (002) orientation is associated with a lower thermodynamic free energy and the tendency to form planar Mg deposits rather than the irregularly-shaped ones,[32–34] suppressing nonuniform Mg deposition and side reactions on the Mg anode surface. With this relationship between the Mg deposits' crystal structure and microstructure, constructing Mg deposits with the preferential (002) orientation may be a promising strategy to promote Mg reversibility, though this is yet to be widely studied in Mg batteries. Recently, epitaxial electrocrystallization of Mg was realized onto a 3D magnesiophilic host *via* a low lattice geometrical misfit between the Mg (002) plane and crystallographic $Ni(OH)_2$ grown on the host.[35] Although lamellar Mg electrodeposits are uniformly formed across the entire architecture of the host, the relatively low intensity of the (002) crystal plane from the X-ray diffraction (XRD) patterns raises questions about the connection between the deposition morphology and the preferential orientations. Therefore, understanding and manipulating Mg crystallography to control the morphology of Mg deposits remain relatively unexplored and warrant further investigation.

In this work, for the first time we introduce a covalent molecule of 1-chloropropane (CP) into conventional electrolytes for reversible and durable Mg metal batteries. Based on the experimental results, COMSOL simulations and density functional theory (DFT) calculations, the dominant effects of CP can be summarized as follows: (1) it enables a robust Cl-rich interphase layer *in situ* formed on Mg electrode surface, minimizing electrolyte decomposition whilst facilitating the electrochemical reaction kinetics. (2) The interaction between CP and Mg electrode reduces the surface energy of Mg (002) crystal plane, enabling preferential electrodeposition of horizontally arranged platelet morphology with enhanced (002) orientations. The addition of CP into magnesium triflate ($Mg(OTf)_2$)-based electrolyte achieves reversible Mg deposition/dissolution and good cycling stability at an unprecedented current density of 25 mA cm^{-2}, the highest value reported to date. Additionally, the CP is also effective for other conventional Mg salts (such as $Mg(TFSI)_2$ and $Mg(HMDS)_2$), indicating its versatility for different Mg electrolytes. The full cells assembled with different cathode materials (Mo_6S_8 and 3,4,9,10-perylenetetracarboxylic dianhydride (PTCDA)) deliver satisfactory cycling performance, exhibiting good compatibility for RMB applications.

Results and discussion

Suppressed surface passivation originating from the *in situ* formed interphase

Coulombic efficiency (CE) is one of the most important parameters reflecting the reversibility of Mg deposition behaviours in electrolytes.[36] Low CE values are usually observed in conventional electrolytes under normal working conditions (Fig. S1, ESI†), indicating significant consumption of Mg ions and solvents due to the aforementioned severe passivation between Mg electrodes and electrolytes. To alleviate this problem, chloride-containing electrolytes have been developed, achieving reversible Mg electrochemical behaviours.[37,38] However, these electrolytes face severe drawbacks including poor anodic stability and corrosion on conventional current collectors (including Al and stainless steel (SS)), arising from dissociated chloride ions, thereby impeding their adoption.[19,39] Encouragingly, CP, an organic molecule with a covalently bonded chlorine atom, is found to have remarkable effects on improving the reversibility of Mg plating/stripping and cycling stability for conventional electrolytes.

The addition of CP with different amounts in $Mg(OTf)_2$ electrolyte were evaluated using asymmetric/symmetric cells (Fig. S2–S4, ESI†), from which 5.4 vol% of CP is regarded as the optimal amount in this work, and 0.2 M $Mg(OTf)_2$ + 5.4 vol% CP is described as $Mg(OTf)_2$ + CP hereinafter.

According to the linear sweep voltammetry (LSV) measurement, the oxidation potentials of $Mg(OTf)_2$ + CP electrolyte on different metal electrodes (Al, SS and Pt) (Fig. S5a, ESI†) are similar to the measured potentials in pure $Mg(OTf)_2$ electrolyte (Fig. S6a, ESI†). This indicates that the addition of CP has a negligible influence on the electrolyte's anodic stability. In addition, highly reversible Mg plating/stripping behaviours in $Mg(OTf)_2$ + CP electrolyte (Fig. S5b, ESI†) are verified by the cyclic voltammetry (CV) (the working electrode is Al). The almost overlapping CV curves over different cycles, coupled with the galvanostatic cycling performance of the asymmetric cells, highlight the superior cycling stability of $Mg(OTf)_2$ + CP electrolyte.

Raman spectroscopy was conducted to investigate the influence of CP addition on the solvation structure of electrolytes. As shown in Fig. 1(a) and Fig. S7 (ESI†), with the dissolution of $Mg(OTf)_2$ in the 1,2-dimethoxyethane (DME) solvent, a blue shift of the DME peak from 867.6 to 870.2 cm^{-1} is observed, indicating the Mg^{2+} coordinated DME in $Mg(OTf)_2$/DME electrolyte.[40] With the addition of CP, the free CP peak at 856.1 cm^{-1} shifts to 864.5 cm^{-1} towards Mg^{2+}-coordinated CP, suggesting that CP is incorporated into the solvation structure.[41] In addition, the peak of coordinated DME shifts to a higher wavenumber (874.1 cm^{-1}), reflecting a structural change of the complex with the coordination of CP molecules.[42] As for the peaks related to anion coordination in the 1010–1070 cm^{-1} region (Fig. S8, ESI†), an apparent shift from 1051.6 to 1043.2 cm^{-1} is observed for the coordinated OTf^- ions after the CP addition in $Mg(OTf)_2$/DME electrolyte, implying a weakening of Mg^{2+}–OTf^- interactions.[42,43] This may enhance the mobility of Mg ions during plating/stripping processes.[44,45]

Another key factor affecting the plating/stripping behaviour of metal anodes is the interface between the electrode and electrolyte.[47,48] Notably, the CEs in the electrolytes with CP all display increasing trends within the first 10 cycles (the inset in Fig. S2, ESI†), which may be associated with the interfacial engineering upon CP addition for Mg deposition.[21,46] Therefore, electrochemical impedance spectroscopy (EIS) was utilized to investigate the interfacial properties of Mg electrodes in different electrolytes. Consistent with prior literatures, the overall interface resistance of the pre-cycled cell in pure $Mg(OTf)_2$ electrolyte is very high (Fig. S9a, ESI†),[49] which is attributed to the formation of an ionically-insulating passivation layer at the electrode–electrolyte interface.[18] This interface resistance is observed to be greatly reduced with the addition of CP, reflecting CP's role in inhibiting surface passivation. Upon cycling, a new semicircle appears in the EIS spectra from the cell using $Mg(OTf)_2$ + CP electrolyte (Fig. S9b, ESI†), which is ascribed to the contribution from a newly formed interphase during cycling.[50] Fitting with equivalent electrical circuit models (the inset in Fig. S9b, ESI†) reveals the resistance of ion migration through the newly formed solid–electrolyte interphase (R_{SEI}) after 100 cycles to be merely 56.31 Ω (Table S1, ESI†), suggesting that the *in situ* formed SEI during the cycling is favorable for electrochemical reactions.

The X-ray photoelectron spectroscopy (XPS) analyses were used to reveal the chemical compositions of the interphases formed on the Mg electrode surface in different electrolytes. After cycling in pure $Mg(OTf)_2$ electrolyte, the surface of Mg electrode is covered by the decomposition products from Mg salt (MgO, MgF_2 and MgS_x) and organic solvent (C–H/C–C, C–O and O═C–O) (Fig. S10 and S11a, ESI†).[18,41,51] The high intensities of these peaks were maintained even after 300 s of Ar etching, which reflects the existence of a thick passivation layer due to self-amplification, where the ionically-insulating passivation layer increases the cell's overpotential, exacerbating the electrolyte decomposition during cycling.[18] In contrast, for the cycled Mg electrode in $Mg(OTf)_2$ + CP electrolyte, the intensities of F 1s, S 2p and C 1s XPS peaks are significantly lower (Fig. 1(d) and Fig. S11b, S12, ESI†), corroborating observations of inhibited passivation with CP addition. Notably, a strong XPS signal of Cl 2p can be observed from the cycled Mg electrode in the $Mg(OTf)_2$ + CP electrolyte (Fig. 1(c)), confirming that CP (the sole Cl source in the electrolyte) actively contributed to the formation of SEI. The formed $MgCl_2$ component in SEI is commonly considered to be Mg^{2+}-conductive and may improve the ion migration at the interface between electrode and electrolyte,[13,52] in accordance with the EIS results (Fig. S9, ESI†). This *in situ* formed SEI can inhibit the surface passivation on the Mg electrode and lead to the highly reversible Mg plating/stripping in $Mg(OTf)_2$ + CP electrolyte (Fig. S2, ESI†). To understand the reaction pathway of the SEI formed *in situ*, molecular orbital energies of individual species and cation (Mg^{2+}) coordinated complexes were calculated by DFT. For the individual species (Fig. 1(e)), the CP molecule has a much lower lowest unoccupied molecular orbital (LUMO) energy level (−0.26 eV) than both DME (1.28 eV) and $Mg(OTf)_2$ (6.94 eV), suggesting a greater propensity to be reduced relative to other species in the electrolyte.[18,53] This tendency is maintained when applied into the Mg^{2+} coordinated complexes, even though the LUMO energy levels of Mg^{2+} coordinated complexes are largely reduced relative to those individual uncoordinated species (Fig. 1(f)). The calculation results indicate a preferential reduction of CP to form the Cl-rich interphase *in situ* on the electrode surface, consistent with the experimental results from XPS.

To further probe its interfacial structure, cryogenic transmission electron microscopy (cryo-TEM) was utilized to directly observe the *in situ* formed Cl-rich interphase on Mg deposits. The TEM sample was prepared by directly plating the Mg deposits onto the TEM Cu grid in $Mg(OTf)_2$ + CP electrolyte. The TEM image in Fig. 1(h) displays a hexagonal morphology of Mg deposits in $Mg(OTf)_2$ + CP electrolyte, with the enlarged image from the edge revealing that the particle comprises numerous platelets (Fig. 1(i)). A uniform layer with a continuous structure is observed on the surface of the plates, with a thickness of ∼3 nm (Fig. 1(j)). The energy dispersive X-ray spectroscopy (EDS) mapping was employed to further unveil the fine structure and elemental composition of the SEI layer. As shown in Fig. S13 (ESI†), the signals of Mg, Cl, C, O, F and S

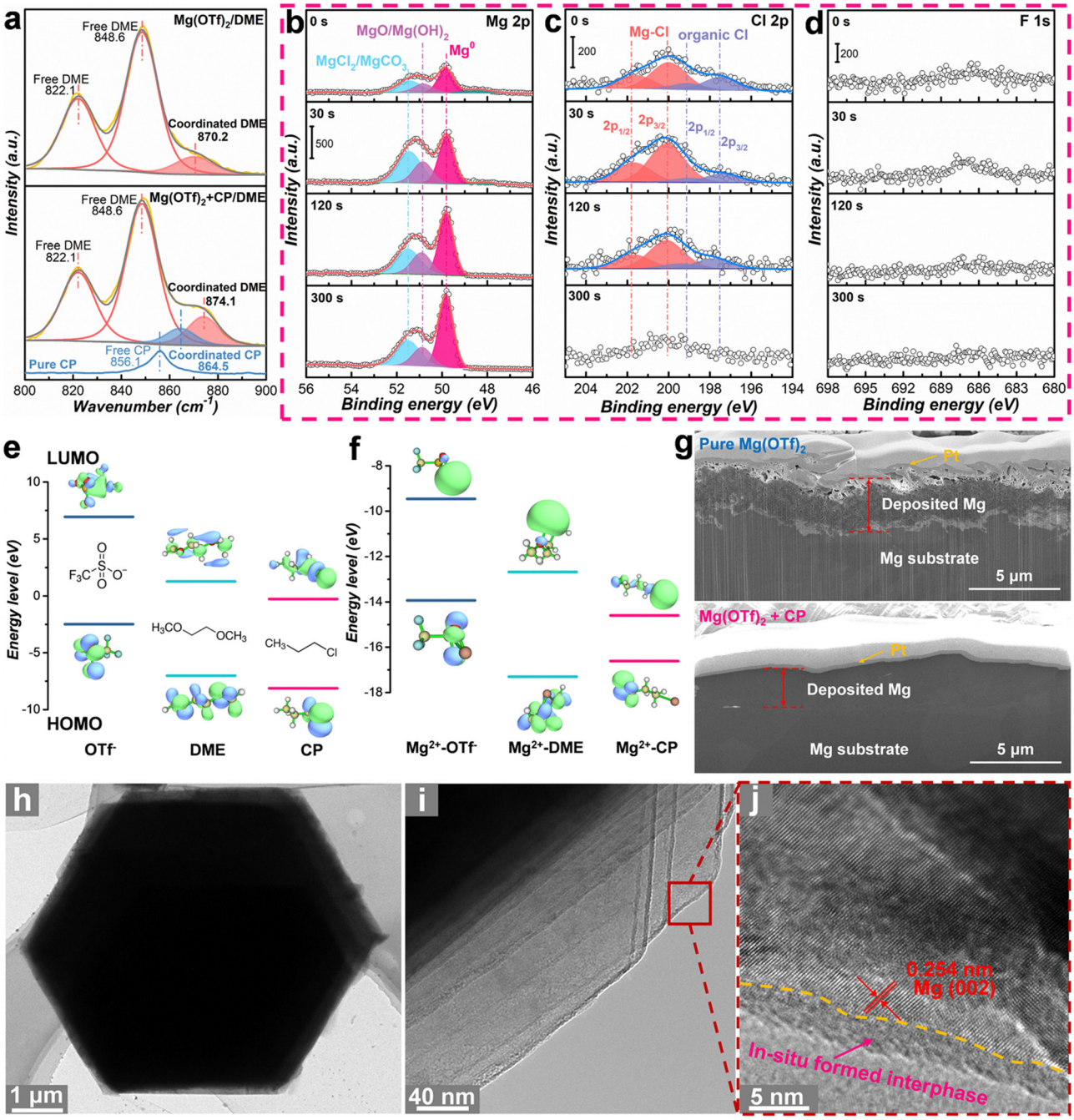

Fig. 1 (a) Raman spectra of $Mg(OTf)_2$/DME, CP liquid and $Mg(OTf)_2$ + CP/DME. XPS spectra of (b) Mg 2p, (c) Cl 2p, and (d) F 1s of the cycled Mg electrode in $Mg(OTf)_2$ + CP electrolyte with different Ar etching times. The calculated LUMO and HOMO energy values of (e) individual species and (f) Mg^{2+} coordinated complexes in $Mg(OTf)_2$ + CP electrolyte. (g) FIB-SEM cross-sectional images of cycled Mg electrodes in pure $Mg(OTf)_2$ and $Mg(OTf)_2$ + CP electrolytes, respectively. The purpose of Pt deposition is to protect the electrode from ion beam damage during sample preparation. (h) and (i) Cryo-TEM images with different magnifications and (j) Cryo-HRTEM image of the surface interphase from the Mg deposit in $Mg(OTf)_2$ + CP electrolyte.

are evenly distributed across the whole architecture of the Mg deposits. It should be noted that the higher intensity of the Cl element (pink) in the edge region of the EDS image, demonstrates that the corresponding interphase is richer in Cl-containing compounds, further supporting CP's involvement in the formation reaction of the interphase on Mg surface.

The suppressed passivation by the CP addition can be directly observed by scanning electron microscopy (SEM; Fig. S14 and S15, ESI†). The Mg anode cycled in pure $Mg(OTf)_2$ electrolyte is covered by irregular products (Fig. S14a and b, ESI†), originating from the significant decomposition of electrolyte, as confirmed by the high amounts of C, S and F elements (Fig. S14c and d, ESI†) obtained from the EDS analysis. In contrast, the Mg electrode cycled in $Mg(OTf)_2$ + CP electrolyte displays a clean and smooth surface (Fig. S15a and b, ESI†) with low amounts of decomposition products from

electrolyte (containing C, S and F elements) (Fig. S15c and d, ESI†), further verifying the hypothesis of the suppressed side reactions between Mg electrode and electrolyte with CP addition. Moreover, with the focused-ion-beam (FIB) treatment, the original cross-sectional view of the cycled Mg electrodes in different electrolytes can be investigated. As shown in Fig. 1(g), a flat and compact morphology is displayed from the cycled electrode in $Mg(OTf)_2$ + CP electrolyte, in contrast to the loosely-packed morphology in pure $Mg(OTf)_2$ electrolyte. Such highly-dense and dendrite-free Mg deposition morphology indicates a well-regulated volumetric change during cycling to greatly enhance the cycling performance. Similar conclusions can also be drawn from time-of-flight-secondary ion mass spectrometry (TOF-SIMS) results (Fig. S16 and S17, ESI†), in which the MgO_2^-, MgF^-, MgS^- and $C_2H_3O^-$ signals (main products from electrolyte decomposition)[54] detected on the cycled Mg electrode in $Mg(OTf)_2$ + CP electrolyte are greatly reduced relative to those in pure $Mg(OTf)_2$ electrolyte. Notably, the distribution profile of the Cl^- signal (Fig. S18, ESI†) is consistent with the presence of Cl observed from the XPS and EDS mapping results, verifying the formation of the Cl-contained interphase on the surface of the cycled Mg electrode in $Mg(OTf)_2$ + CP electrolyte.

To validate the robustness of the *in situ* formed SEI, the interphase was intentionally constructed on the Mg electrodes through the pre-cycling in $Mg(OTf)_2$ + CP electrolyte. Subsequently, the two Mg electrodes were disassembled from the cycled symmetric cell, thoroughly washed with DME solvent, and re-assembled in a separate Mg//Mg cell using pure $Mg(OTf)_2$ electrolyte. Surprisingly, the Mg electrodes protected with SEI exhibit a much lower overpotential of approximately 0.4 V after stable cycling over 250 h in pure $Mg(OTf)_2$ electrolyte, in contrast to the large overpotentials and poor cycling performance of bare Mg with the same electrolyte (Fig. S19, ESI†). We highlight that when pre-cycled with other commonly-used electrolytes (such as the all phenyl complex (APC)[55] and $Mg(OTf)_2$ + $MgCl_2$[51] electrolytes), the cycled Mg electrodes do not allow for stable cycling when re-assembled into pure $Mg(OTf)_2$ cells (Fig. S20, ESI†), thereby reflecting the robustness and uniqueness of the *in situ* formed SEI in $Mg(OTf)_2$ + CP electrolyte.

Horizontal Mg platelet deposition enabled by the CP addition

In addition to the inhibited passivation due to the *in situ* formed SEI, the deposition morphology is also crucial for the cycling performance of Mg batteries. The non-uniform Mg deposition is concomitant with rapid electrolyte depletion, poor cycling performance, and potential safety hazards.[24] These issues plaguing Mg batteries necessitate a better understanding of Mg deposition morphologies in different electrolytes. In pure $Mg(OTf)_2$ electrolyte (Fig. 2(a1)), a porous morphology arising from the accumulation of whisker-shaped Mg dendrites is observed at 0.5 mA cm^{-2}, intensifying the surface roughness and pulverization risk.[53] In contrast, the Mg deposits in $Mg(OTf)_2$ + CP electrolyte exhibit a planar platelet morphology, and are well-stacked on the substrate surface, forming a smooth surface profile and strong adhesion to the current collector (Fig. 2(b1)). Further increasing the current density to 1.0 mA cm^{-2} yields similar morphological characteristics of the Mg deposits in these two electrolytes (Fig. 2(c1) and (d1)). Supporting SEM micrographs comparing the morphologies upon addition of CP with different magnifications are presented in Fig. S21–S24 (ESI†). The formation of Mg dendrites (Fig. 2(a1) and (c1)) significantly increases the specific surface area of Mg electrode, thereby accelerating the parasitic reactions with electrolyte and exhausting the Mg sources, exacerbating the poor reversibility of Mg anodes alongside potential safety hazards.[56,57] In contrast, the horizontally arranged platelets morphology of Mg deposits in $Mg(OTf)_2$ + CP electrolyte significantly relieves the severe safety concerns arising from dendritic Mg deposits. Unlike typical dendrites formed in pure $Mg(OTf)_2$ electrolyte, which are several micrometers long and may penetrate the separators easily, the platelet structures avoid the possible penetration through the separators and consequent short circuits. Additionally, the compactly packed Mg deposits in $Mg(OTf)_2$ + CP electrolyte possess a much smaller specific surface area, minimizing the side reactions between Mg deposits and electrolyte,[58] and contributing to the enhanced Mg plating/stripping CEs observed in Fig. S2 (ESI†). The horizontally arranged platelet morphology of Mg deposits in $Mg(OTf)_2$ + CP electrolyte is further corroborated from the atomic force microscopy (AFM) measurements (Fig. S25 and S26, ESI†). The average height differences (along the X and Y axis) of Mg deposits at 0.5 and 1.0 mA cm^{-2} are only 162.5 and 88.5 nm, respectively, further confirming the flat and uniform Mg deposition in $Mg(OTf)_2$ + CP electrolyte.

In addition to the advantageous platelet morphology, the $Mg(OTf)_2$ + CP electrolyte also displays significantly enhanced signals of Mg (002) crystal planes relative to pure $Mg(OTf)_2$ electrolyte according to the XRD patterns (Fig. 2(a2)–(d2)) and 2D wide-angle X-ray scattering (WAXS) plots (Fig. 2(a3)–(d3)). Specifically, a higher XRD intensity of Mg (002) arises from the horizontally-oriented Mg deposits arranged on the substrate.[27] The increased intensity of the (002) crystal plane implies that the addition of CP may alter the orientation of Mg deposits, which is quantified by calculating the intensity ratio between Mg (002) and Mg (100) peaks. As displayed in Fig. S27 (ESI†), the $I_{(002)}/I_{(100)}$ ratios of Mg deposits in the $Mg(OTf)_2$ + CP electrolyte are 4.10 (0.5 mA cm^{-2}) and 4.05 (1 mA cm^{-2}), which are much higher than those in pure $Mg(OTf)_2$ electrolyte of 0.76 (0.5 mA cm^{-2}) and 0.48 (1 mA cm^{-2}). The above results verify the enhanced (002) orientation of the Mg deposits induced by CP addition, which are consistent with the observations from microscopy experiments.

Performance evaluation of the reversible and durable Mg metal batteries

The suppressed surface passivation and horizontally arranged Mg platelet deposition enabled by the CP addition are expected to dramatically enhance the electrochemical performance of Mg batteries. As presented in Fig. 3(a), the Mg//Al cell using $Mg(OTf)_2$ + CP electrolyte displays excellent reversibility and rate capability at different current densities. Remarkably, even

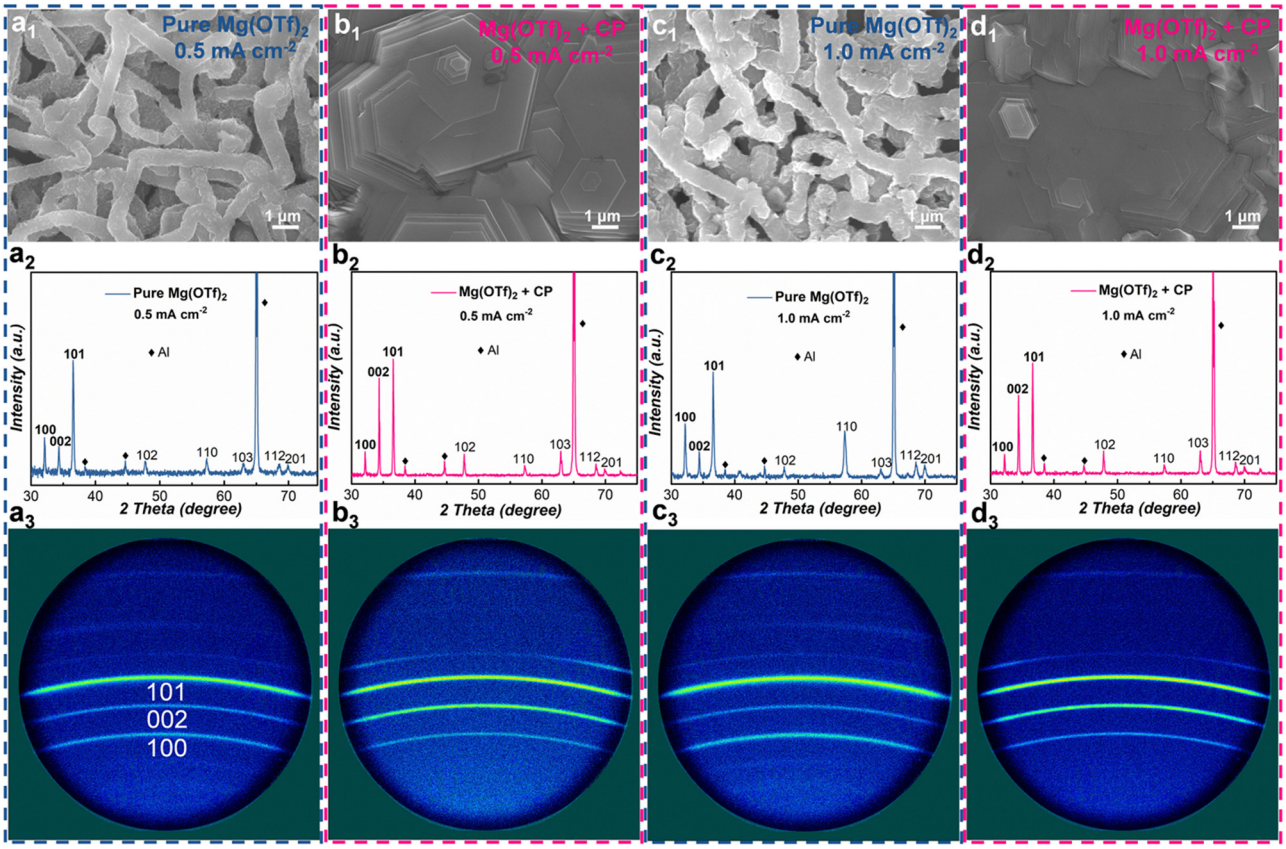

Fig. 2 Morphology, crystallography and microstructure characterizations of Mg deposits. SEM images of Mg deposits in (a_1), (c_1) pure $Mg(OTf)_2$ electrolyte and (b_1), (d_1) $Mg(OTf)_2$ + CP electrolyte; XRD patterns of Mg deposits in (a_2), (c_2) pure $Mg(OTf)_2$ electrolyte and (b_2), (d_2) $Mg(OTf)_2$ + CP electrolyte; 2D WAXS results of Mg deposits in (a_3), (c_3) pure $Mg(OTf)_2$ electrolyte and (b_3), (d_3) $Mg(OTf)_2$ + CP electrolyte at different current densities of 0.5 mA cm^{-2} and 1 mA cm^{-2}, respectively.

at an ultrahigh current density of 30 mA cm^{-2}, $Mg(OTf)_2$ + CP electrolyte still achieves reversible Mg plating/stripping with an outstanding average CE of 99.68%. To further verify the stellar reversibility in $Mg(OTf)_2$ + CP electrolyte, long-term stability tests were conducted under different working conditions. At a moderate current density (1 mA cm^{-2}, Fig. 3(c) and Fig. S28, ESI†), the asymmetric cell with $Mg(OTf)_2$ + CP electrolyte delivers a high and stable CE with an average value up to 99.67% over 900 cycles. In contrast, the pure $Mg(OTf)_2$ electrolyte displays fluctuating CEs with a much lower average value of 64.96% across only 14 cycles. The selected voltage profiles are displayed in Fig. 3(d) and (e), where the $Mg(OTf)_2$ + CP electrolyte delivers almost overlapped profiles and low voltage hysteresis, while the pure $Mg(OTf)_2$ electrolyte shows a large voltage drop due to the exacerbated passivation. High current densities typically increase the probability of dendrite formation and thus are detrimental to the reversibility of plating/stripping.[24,42] Despite this, the $Mg(OTf)_2$ + CP electrolyte still achieves remarkable average CE values of 99.82% and 99.81% over 1000 and 1600 cycles at 5 and 10 mA cm^{-2}, respectively (Fig. S29 and S30, ESI†). Encouragingly, even under an ultrahigh current density of 25 mA cm^{-2} (Fig. S31, ESI†), an average CE of 99.79% is achieved over ~4000 cycles. Moreover, the average CE value can still be maintained at 99.61% over 640 cycles when the capacity is increased to 2 mA h cm^{-2} (at 20 mA cm^{-2}) (Fig. S32, ESI†). These exceptional performances of the $Mg(OTf)_2$ + CP electrolyte present a significant improvement from recent literatures as summarized in Table S2 (ESI†). The encouraging performances inspire us to further explore the maximum plating capacity *via* stepwise increments in capacity from 1 up to 15 mA h cm^{-2}, where the CE of the cell with $Mg(OTf)_2$ + CP electrolyte is maintained at nearly 99.59% (Fig. S33, ESI†).

The remarkable electrochemical performance of the $Mg(OTf)_2$ + CP electrolyte was also evaluated using symmetrical cells, demonstrating stable cycling over a wide range of current densities from 1 up to 30 mA cm^{-2} (Fig. 3(b)). Additionally, galvanostatic cycling was conducted in Mg//Mg cells to evaluate the durability of the electrolytes. The $Mg(OTf)_2$ + CP electrolyte enables a prolonged cycling life over 1700 h at 1 mA cm^{-2} and 1 mA h cm^{-2}, compared to a mere 12 h cycling lifespan of the pure $Mg(OTf)_2$ electrolyte (Fig. S34, ESI†). Moreover, the $Mg(OTf)_2$ + CP electrolyte displays an ultralow voltage hysteresis of ~110 mV at 1 mA cm^{-2}, which is mainly attributed to the elevated Mg plating/stripping kinetics originating from the *in situ* formed SEI, as verified by the exchange current density (j_0) (Fig. S35, ESI†). The j_0 in $Mg(OTf)_2$ + CP electrolyte reaches 107.3 μA cm^{-2}, which is much higher than the value of 0.0284 μA cm^{-2} in pure $Mg(OTf)_2$ electrolyte, revealing the

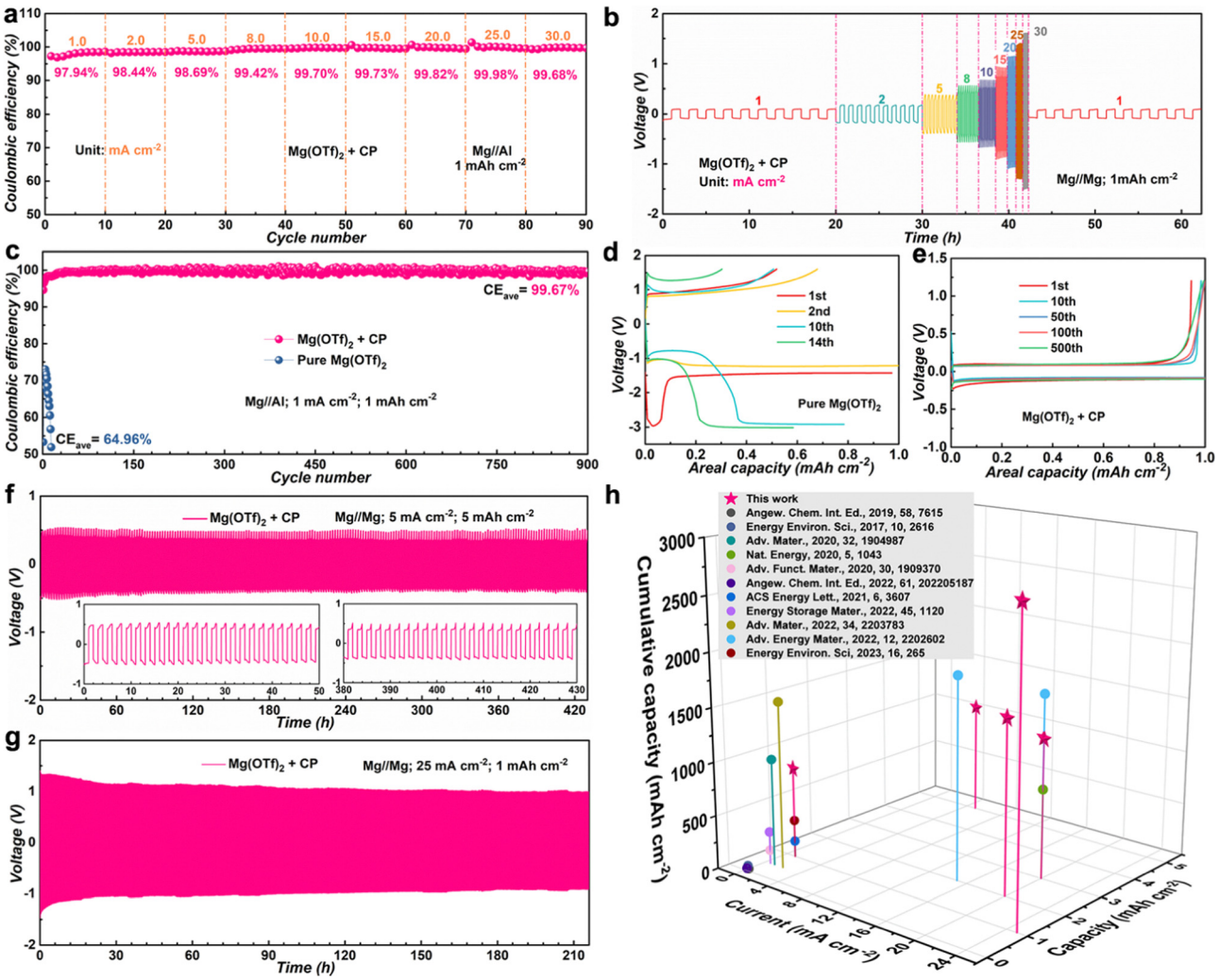

Fig. 3 The electrochemical performance of Mg metal batteries with $Mg(OTf)_2$ + CP electrolyte. (a) The CE values of the asymmetric cell and (b) voltage profiles of the symmetric cell at different current densities from 1 to 30 mA cm^{-2} at 1 mA h cm^{-2}. (c) The CEs of Mg plating/stripping and the selected voltage profiles from different cycles of asymmetric cells in (d) pure $Mg(OTf)_2$ and (e) $Mg(OTf)_2$ + CP electrolytes at 1 mA cm^{-2} and 1 mA h cm^{-2}. High-rate cycling performance of symmetric cells with $Mg(OTf)_2$ + CP electrolytes at (f) 5 mA cm^{-2}/5 mA h cm^{-2} (the insets are corresponding voltage profiles from different cycles) and (g) 25 mA cm^{-2}/1 mA h cm^{-2}. (h) Performance comparison of symmetric cells with previous reported works.

key role of the *in situ* formed interphase in modulating reaction kinetics.[10,52] The horizontally stacked platelet morphology is also well preserved after 500 cycles (Fig. S36, ESI†), suggesting that the flat deposition morphology is also a key contributor to the excellent cycling stability of the Mg anodes. When the working conditions are raised to the target values for practical applications of 3 mA cm^{-2}/3 mA h cm^{-2} and 5 mA cm^{-2}/5 mA h cm^{-2}, the Mg//Mg cells with $Mg(OTf)_2$ + CP electrolyte sustain constant plating/stripping processes without obvious fluctuations for 790 h and 430 h, respectively, as revealed by the flat voltage plateaus in Fig. S37 (ESI†) and Fig. 3(f). On the contrary, the pure $Mg(OTf)_2$ electrolyte does not allow for cycling under such large current densities due to the serious passivation issues. Even upon further ramping of the current density to 25 mA cm^{-2}, the Mg//Mg cells with $Mg(OTf)_2$ + CP electrolyte maintain highly durable cycling for over 215 h (Fig. 3(g) and Fig. S38, ESI†). Moreover, under higher cycling capacity conditions (Fig. S39 and S40, ESI†), including 2 and 3 mA h cm^{-2} at 20 mA cm^{-2}, stable cycling can still be maintained over 160 h and 130 h, respectively. This performance of $Mg(OTf)_2$ + CP electrolyte in symmetrical cells is comparable or even superior to the best-reported results for Mg electrolytes (Fig. 3(h) and Table S3, ESI†). Remarkably, a satisfactory performance was demonstrated with other conventional Mg salts with the addition of CP, such as $Mg(TFSI)_2$ and $Mg(HMDS)_2$ (Fig. S41–S44, ESI†), indicating the versatility of CP for different electrolytes in Mg batteries. Furthermore, a promising performance was achieved with lean $Mg(OTf)_2$ + CP electrolyte (10 μL) (Fig. S45, ESI†), suggesting the potential of the electrolyte to facilitate higher energy density RMBs for practical applications.

Performance evaluation of the full cells assembled with different cathode materials

Encouraged by the promising properties and excellent cycling performance of the $Mg(OTf)_2$ + CP electrolyte, its compatibility

with different cathode materials was investigated. Firstly, the Chevrel phase Mo_6S_8, a representative cathode material, was used to evaluate the potential application of $Mg(OTf)_2$ + CP electrolyte for RMBs. Cyclic voltammetry (Fig. S46, ESI†) indicates that Mg ions intercalate reversibly into the Mo_6S_8 electrode in two stages (with two sets of peaks where the two cathodic peaks overlap), corresponding to the respective plateau regions in the charging/discharging curves. The Mg//Mo_6S_8 cell using $Mg(OTf)_2$ + CP electrolyte exhibits excellent rate capability from 0.1C to 5C (1C = 129 mA g^{-1}), with a discharging capacity of 94.9 mA h g^{-1} at 0.1C and 41.7 mA h g^{-1} maintained at 5C (Fig. 4(a)). Upon switching back to 0.1C, the discharging capacity recovers back to 94.3 mA h g^{-1}, demonstrating the outstanding stability of the $Mg(OTf)_2$ + CP electrolyte. The corresponding charging/discharging curves in Fig. 4(b) reflect the satisfactory voltage plateaus of the Mg//Mo_6S_8 cell at different current densities in $Mg(OTf)_2$ + CP electrolyte. The increasing overpotentials between charging and discharging plateaus under higher current densities imply a reduction of Mg-ion intercalation/deintercalation, attributed to heightened solid state diffusion limitations at higher rates.[59] Long-term cycling performance is further measured at different discharging rates. Impressively, at 0.5C (Fig. 4(c)), the Mg//Mo_6S_8 cell using $Mg(OTf)_2$ + CP electrolyte delivers a reversible capacity of 64.2 mA h g^{-1} after 400 cycles (with a capacity retention of 94.4%). The corresponding charging/discharging curves demonstrate small and stable voltage polarization (inset in Fig. 4(c)). Good stability is obtained even at a high discharging rate of 5C, during which the discharging capacity is stably maintained at ~40.0 mA h g^{-1} for over 2000 cycles, with an average CE value close to 100% (Fig. 4(d)).

To further confirm the compatibility with other cathode materials possessing higher working voltages, an unconventional organic cathode material of PTCDA was utilized.[60,61] A discharging capacity of 113.7 mA h g^{-1} is obtained from the PTCDA electrode at a current density of 25 mA g^{-1} (Fig. S47, ESI†). As current densities are increased, the reversible capacities gradually decrease and the Mg-storage capacities of PTCDA are 82.1, 60.1, and 42.5 mA h g^{-1} at 50, 100, and 200 mA g^{-1}, respectively. Thereafter, the initial capacity is recovered upon returning to 25 mA g^{-1}. The galvanostatic charging/discharging cycling of the Mg//PTCDA cell shows an initial capacity of 80.2 mA h g^{-1} at 50 mA g^{-1}, with the capacity retained at 61.3 mA h g^{-1} after 120 cycles (Fig. 4(e)) alongside an average CE of 95.11%. Consistent with the CV curve (Fig. S48, ESI†), the major discharging and charging plateaus of the Mg//PTCDA cell are located at ~1.65 V and ~2.10 V, respectively (Fig. 4(e), inset), indicative of a higher working voltage relative to Mg//Mo_6S_8. Furthermore, a discharging capacity of 36.2 mA h g^{-1} is retained after 200 cycles at a high current density of 200 mA g^{-1}, with a satisfactory average CE of 98.50% (Fig. S49, ESI†). The above results demonstrate that the as-designed $Mg(OTf)_2$ + CP electrolyte is compatible with different inorganic and organic cathode materials, reflecting its versatile compatibility for RMB applications.

Theoretical simulation and calculation for the dynamic behaviours of Mg deposition

Generally, the dynamic behaviours of Mg deposition are significantly influenced by the distributions of Mg^{2+} flux and electrical field at the interphase between electrode and electrolyte,[49,52] which can be simulated and visualized using the finite element method (FEM) conducted in COMSOL. As shown in Fig. S50 and S51 (ESI†), due to the thick passivation layer formed in pure $Mg(OTf)_2$ electrolyte, concentration polarization is observed at the electrode–electrolyte interphase. Coupled with the limited nucleation sites on the thick passivation layer, this promotes random deposition of protrusions on the Mg electrodes

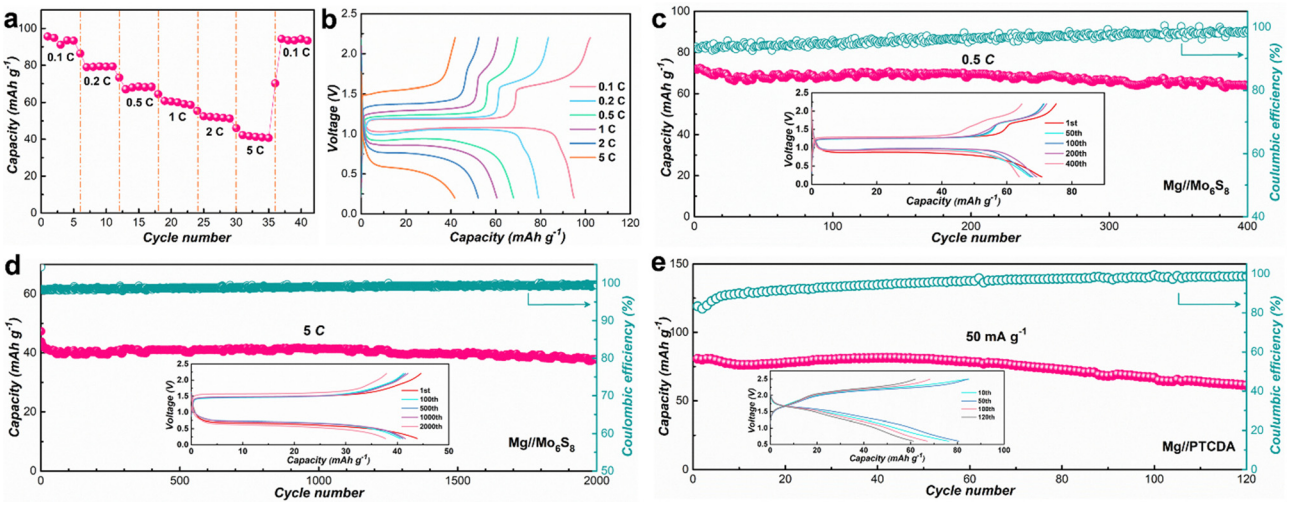

Fig. 4 The performance of Mg//Mo_6S_8 and Mg//PTCDA cells with $Mg(OTf)_2$ + CP electrolyte. (a) Rate performance of Mg//Mo_6S_8 cells from 0.1C to 5C and (b) the corresponding charging/discharging profiles between 0.2 V and 2.2 V (*versus* Mg/Mg^{2+}). (c) Long-term cycling performance of Mg//Mo_6S_8 cells at 0.5C over 400 cycles and (d) stability test at 5C for 2000 cycles. (e) Cycling performance of Mg//PTCDA cells at a current density of 50 mA g^{-1}. The inset shows the selected charging/discharging profiles between 0.6 V and 2.5 V (*versus* Mg/Mg^{2+}).

(Fig. S52a, ESI†). Once such protrusions are formed, the electric field distribution would be distorted, and the local current intensity tends to concentrate around the sharp edges (Fig. 5(a)).[46] This leads to detrimental tip effects with warped distributions of ion concentration alongside "hot spots" of local electric field, further aggravating the non-uniform Mg deposition

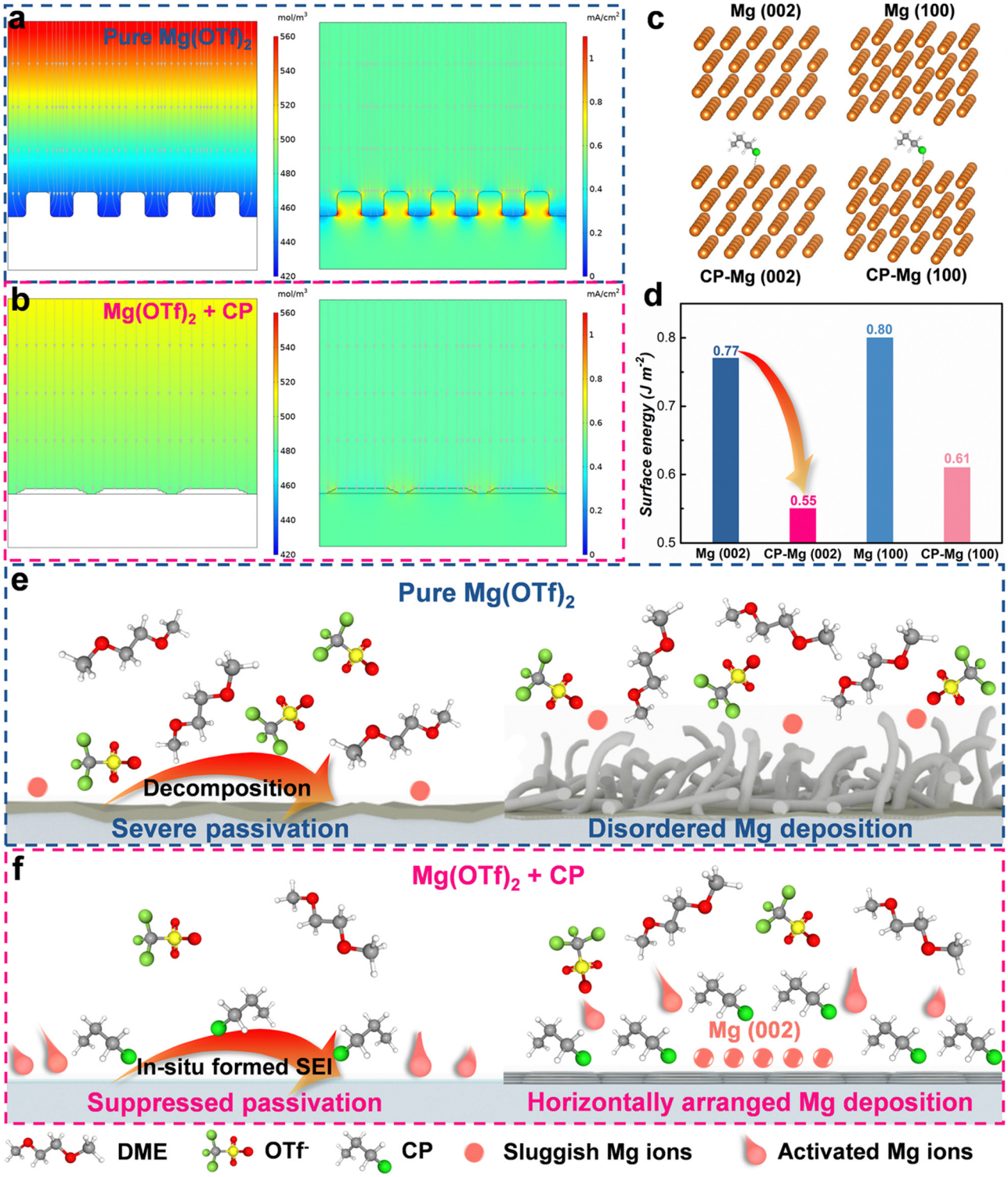

Fig. 5 Theoretical simulation and calculation for the dynamic behaviours of Mg anodes. COMSOL simulations of the Mg^{2+} flux and electrical field distributions in (a) pure $Mg(OTf)_2$ and (b) $Mg(OTf)_2$ + CP electrolytes at 0.5 mA cm^{-2}. (c) Calculations models and (d) surface energy comparison of different crystal planes. Schematic illustrations of electrode–electrolyte interphases and Mg deposition behaviours in (e) pure $Mg(OTf)_2$ and (f) $Mg(OTf)_2$ + CP electrolytes.

and possibly inducing the growth of dendrites.[62] After introducing CP into the electrolyte, Mg-ion flux may be completely redistributed by the *in situ* formed SEI and alleviated passivation effects (Fig. S51b, ESI†), thereby homogenizing the Mg-ion flux and electric field across the whole architecture of the electrode and ultimately leading to smooth Mg deposition (Fig. S52b, ESI†). The flat and dense Mg deposition in $Mg(OTf)_2$ + CP electrolyte would further equalize the Mg-ion flux and reduce the local current density, thus eliminating the tip effects to achieve efficient cycling (Fig. 5(b)).

Fundamentally, regulation of crystal structure is pertinent to influencing metal electrodeposition morphology.[27,28] Since the preferred orientation of crystal planes is closely correlated with the changes in surface energy,[32,63,64] DFT calculations were conducted to understand the surface chemistry on Mg electrodes at a molecular level. According to the calculation of molecular orbital energies in Fig. 1(e), the appropriate LUMO energy level of the CP molecule indicates its strong interaction with the Mg electrode,[18,53] thereby influencing the relative surface energy values of different crystal planes and altering the Mg deposition morphology.[32] To validate this hypothesis, the surface energy of Mg (002) and Mg (100) planes with/without CP addition was studied using DFT calculations (Fig. 5(c)). As shown in Fig. 5(d), the calculated results reveal significant reduction of the surface energy of the (002) crystal plane with CP addition by 0.22 J m^{-2}. This indicates enhanced stability of the Mg (002) plane in the presence of CP, corroborating the XRD results above where the (002) plane orientations are preferentially formed relative to the (100) plane. Although the calculated surface energy of bare Mg (002) is also lower than the Mg (100) in pure $Mg(OTf)_2$ electrolyte, the serious passivation issues alter the surface structure of the Mg metal considerably, thus disrupting the propensity for inheriting its intrinsic orientation.[27]

Based on the above experimental and computational results, the modulation effects of CP for the surface chemistry and Mg deposition behaviours are summarized with a schematic depiction in Fig. 5(e) and (f). In pure $Mg(OTf)_2$ electrolyte, thermodynamically unstable Mg electrodes are susceptible to reactions with the electrolyte components, forming a detrimental Mg^{2+}-insulating passivation film. This unstable interphase incurs the continuous consumption of Mg sources, poor reversibility of Mg plating/stripping and uneven Mg deposition.[11] In contrast, a robust Cl-rich interphase is formed *in situ* on the Mg electrode surface with the addition of CP, which can facilitate the ion migration and prevent electrolyte decomposition on Mg anodes. In addition, the interaction between CP and Mg metal would alter the surface chemistry of Mg electrode, resulting in the significantly reduced surface energy of the Mg (002) plane, allowing enhanced (002) orientation for Mg deposition to be achieved. Overall, the CP contributes toward mitigating unfavorable electrolyte decomposition and enabling the horizontally arranged Mg platelet deposition.

Conclusions

In summary, a covalent molecule of CP is proposed for manipulating the kinetics and surface chemistry of Mg anodes in $Mg(OTf)_2$-based electrolytes, achieving suppressed passivation and horizontally arranged Mg platelet electrodeposition for high-performance Mg metal batteries. As revealed by electrochemical measurements and structural characterization techniques, a robust Cl-rich SEI is formed *in situ* on the Mg electrode surface, effectively minimizing the sustained electrolyte decomposition and facilitating the electrochemical reaction kinetics. In addition, arising from interactions between the CP and Mg electrode, the surface energy of the Mg (002) crystal plane is reduced, promoting the growth of horizontally arranged platelets with enhanced (002) orientations during the electrodeposition process. The protective SEI coupled with the planar deposition morphology allows for highly reversible Mg plating/stripping across a wide current density range (0.5–30 mA cm^{-2}). Remarkable cycling performances are also achieved in symmetric cells, delivering stellar cycling stability for 420 h under working conditions suitable for commercial adoption (5 mA cm^{-2}/5 mA h cm^{-2}) as well as 130 h under the high-rate working conditions (20 mA cm^{-2}/3 mA h cm^{-2}), which are among the best performances compared to prior works. The engineered electrolyte exhibits excellent compatibility with different cathode materials (Mo_6S_8 and PTCDA), offering promising opportunities for RMB applications. Additionally, the CP demonstrates promising performances when adopted with other conventional Mg salts (such as $Mg(TFSI)_2$ and $Mg(HMDS)_2$), reflecting its versatility to be adapted for different Mg electrolytes. Our work highlights the importance of surface/interface modulation *via* electrolyte modification to inhibit passivation and realize planar Mg deposition, and provides new insights for regulating the Mg deposition behaviours through correlating crystallography and morphology.

Author contributions

G. Y., Y. L. and Z. W. S. conceived the idea. G. Y. prepared the manuscript and performed the experiments. G. Y., Y. L. and Z. C. conducted the data analysis. J. W. conducted the XRD characterization. C. Y. J. L., Y. Y. and Z. W. S. revised the manuscript. M. F. N., Z. Z. and S. L. conducted the DFT calculations. C. Z. and W. L. performed the COMSOL simulations. A. D. H. conducted the 2D WAXS characterization. T. G. conducted the cryo-TEM characterization. Z. S. provided the Mo_6S_8 cathode materials. Z. W. S. supervised the project. All authors discussed the results and commented on the manuscript.

Conflicts of interest

There are no conflicts to declare.

Acknowledgements

Z. W. S. acknowledges the Agency for Science, Technology and Research (Central Research Fund Award). M.-F. N. acknowledges the National Supercomputing center (NSCC) Singapore and A*STAR Computational Resource center (A*CRC) of Singapore through the use of its high-performance computing

facilities. Z. S. acknowledges the Czech Science Foundation (GACR no. 20-16124J). The authors acknowledge Dr Hwee Leng Debbie Seng, Mr Zhenxiang Xing and Ms Xue Qi Koh of Institute of Materials Research and Engineering for their assistance in performing the initial XPS, TOF-SIMS and AFM measurements. The authors also thank Dr Teck Lip Dexter Tam and Mr Zi Hui Jonathan Khoo for their productive and helpful discussions.

References

1 Y. Tian, G. Zeng, A. Rutt, T. Shi, H. Kim, J. Wang, J. Koettgen, Y. Sun, B. Ouyang, T. Chen, Z. Lun, Z. Rong, K. Persson and G. Ceder, *Chem. Rev.*, 2021, **121**, 1623–1669.
2 A. Y. S. Eng, C. B. Soni, Y. Lum, E. Khoo, Z. Yao, S. K. Vineeth, V. Kumar, J. Lu, C. S. Johnson, C. Wolverton and Z. W. Seh, *Sci. Adv.*, 2022, **8**, eabm2422.
3 J. W. Choi and D. Aurbach, *Nat. Rev. Mater.*, 2016, **1**, 16013.
4 J. Muldoon, C. B. Bucur and T. Gregory, *Chem. Rev.*, 2014, **114**, 11683–11720.
5 Y. Liang, H. Dong, D. Aurbach and Y. Yao, *Nat. Energy*, 2020, **5**, 646–656.
6 Z. Guo, S. Zhao, T. Li, D. Su, S. Guo and G. Wang, *Adv. Energy Mater.*, 2020, **10**, 1903591.
7 J. Zhang, Z. Chang, Z. Zhang, A. Du, S. Dong, Z. Li, G. Li and G. Cui, *ACS Nano*, 2021, **15**, 15594–15624.
8 J. Zhang, J. Liu, M. Wang, Z. Zhang, Z. Zhou, X. Chen, A. Du, S. Dong, Z. Li, G. Li and G. Cui, *Energy Environ. Sci.*, 2023, **16**, 1111–1124.
9 J. Bae, H. Park, X. Guo, X. Zhang, J. H. Warner and G. Yu, *Energy Environ. Sci.*, 2021, **14**, 4391–4399.
10 Y. Zhang, J. Li, W. Zhao, H. Dou, X. Zhao, Y. Liu, B. Zhang and X. Yang, *Adv. Mater.*, 2022, **34**, e2108114.
11 Z. Liang and C. Ban, *Angew. Chem., Int. Ed.*, 2021, **60**, 11036–11047.
12 R. Lv, X. Guan, J. Zhang, Y. Xia and J. Luo, *Natl. Sci. Rev.*, 2020, **7**, 333–341.
13 Y. Zhao, A. Du, S. Dong, F. Jiang, Z. Guo, X. Ge, X. Qu, X. Zhou and G. Cui, *ACS Energy Lett.*, 2021, **6**, 2594–2601.
14 X. Li, T. Gao, F. Han, Z. Ma, X. Fan, S. Hou, N. Eidson, W. Li and C. Wang, *Adv. Energy Mater.*, 2017, **8**, 1701728.
15 D. Chinnadurai, W. Y. Lieu, S. Kumar, G. Yang, Y. Li and Z. W. Seh, *Nano Lett.*, 2023, **23**, 1564–1572.
16 S. B. Son, T. Gao, S. P. Harvey, K. X. Steirer, A. Stokes, A. Norman, C. Wang, A. Cresce, K. Xu and C. Ban, *Nat. Chem.*, 2018, **10**, 532–539.
17 R. Zhang, C. Cui, R. Li, Y. Li, C. Du, Y. Gao, H. Huo, Y. Ma, P. Zuo and G. Yin, *Chem. Eng. J.*, 2021, **426**, 130751.
18 J. Xiao, X. Zhang, H. Fan, Y. Zhao, Y. Su, H. Liu, X. Li, Y. Su, H. Yuan, T. Pan, Q. Lin, L. Pan and Y. Zhang, *Adv. Mater.*, 2022, **34**, e2203783.
19 Y. Sun, F. Ai and Y. C. Lu, *Small*, 2022, e2200009.
20 X. Zeng, J. Mao, J. Hao, J. Liu, S. Liu, Z. Wang, Y. Wang, S. Zhang, T. Zheng, J. Liu, P. Rao and Z. Guo, *Adv. Mater.*, 2021, **33**, 2007416.
21 H. Qiu, X. Du, J. Zhao, Y. Wang, J. Ju, Z. Chen, Z. Hu, D. Yan, X. Zhou and G. Cui, *Nat. Commun.*, 2019, **10**, 5374.
22 X. Cao, X. Ren, L. Zou, M. H. Engelhard, W. Huang, H. Wang, B. E. Matthews, H. Lee, C. Niu, B. W. Arey, Y. Cui, C. Wang, J. Xiao, J. Liu, W. Xu and J.-G. Zhang, *Nat. Energy*, 2019, **4**, 796–805.
23 P. Bonnick and J. Muldoon, *Adv. Funct. Mater.*, 2020, **30**, 1910510.
24 J. Eaves-Rathert, K. Moyer, M. Zohair and C. L. Pint, *Joule*, 2020, **4**, 1324–1336.
25 J. H. Um, S.-J. Kim, J.-H. Hyun, M. Kim, S.-H. Lee and S.-H. Yu, *Acc. Chem. Res.*, 2023, **56**, 440–451.
26 K. Popov, B. Grgur and S. S. Djokić, *Fundamental aspects of electrometallurgy*, Springer, 2007.
27 J. Zheng and L. A. Archer, *Chem. Rev.*, 2022, **122**, 14440–14470.
28 J. Zheng and L. A. Archer, *Sci. Adv.*, 2021, **7**, eabe0219.
29 J. Zheng, M. S. Kim, Z. Tu, S. Choudhury, T. Tang and L. A. Archer, *Chem. Soc. Rev.*, 2020, **49**, 2701–2750.
30 M. Jäckle and A. Groß, *J. Chem. Phys.*, 2014, **141**, 174710.
31 J. L. Esbenshade, C. J. Barile, T. T. Fister, K. L. Bassett, P. Fenter, R. G. Nuzzo and A. A. Gewirth, *J. Phys. Chem. C*, 2015, **119**, 23366–23372.
32 Z. Zhao, R. Wang, C. Peng, W. Chen, T. Wu, B. Hu, W. Weng, Y. Yao, J. Zeng, Z. Chen, P. Liu, Y. Liu, G. Li, J. Guo, H. Lu and Z. Guo, *Nat. Commun.*, 2021, **12**, 6606.
33 J. Zheng, Q. Zhao, T. Tang, J. Yin, C. D. Quilty, G. D. Renderos, X. Liu, Y. Deng, L. Wang, D. C. Bock, C. Jaye, D. Zhang, E. S. Takeuchi, K. J. Takeuchi, A. C. Marschilok and L. A. Archer, *Science*, 2019, **366**, 645–648.
34 M. Matsui, *J. Power Sources*, 2011, **196**, 7048–7055.
35 J. Liu, J. Zhang, Z. Zhang, A. Du, S. Dong, Z. Zhou, X. Guo, Q. Wang, Z. Li, G. Li and G. Cui, *ACS Nano*, 2022, **16**, 9894–9907.
36 J. Xiao, Q. Li, Y. Bi, M. Cai, B. Dunn, T. Glossmann, J. Liu, T. Osaka, R. Sugiura, B. Wu, J. Yang, J.-G. Zhang and M. S. Whittingham, *Nat. Energy*, 2020, **5**, 561–568.
37 R. Mohtadi, O. Tutusaus, T. S. Arthur, Z. Zhao-Karger and M. Fichtner, *Joule*, 2021, **5**, 581–617.
38 H. Zhang, L. Qiao and M. Armand, *Angew. Chem., Int. Ed.*, 2022, **61**, e202214054.
39 J. Muldoon, C. B. Bucur, A. G. Oliver, J. Zajicek, G. D. Allred and W. C. Boggess, *Energy Environ. Sci.*, 2013, **6**, 482–487.
40 W. Zhao, Z. Pan, Y. Zhang, Y. Liu, H. Dou, Y. Shi, Z. Zuo, B. Zhang, J. Chen, X. Zhao and X. Yang, *Angew. Chem., Int. Ed.*, 2022, **61**, e202205187.
41 Y. Sun, Y. Wang, L. Jiang, D. Dong, W. Wang, J. Fan and Y.-C. Lu, *Energy Environ. Sci.*, 2023, **16**, 265–274.
42 D.-T. Nguyen, A. Y. S. Eng, R. Horia, Z. Sofer, A. D. Handoko, M.-F. Ng and Z. W. Seh, *Energy Storage Mater.*, 2022, **45**, 1120–1132.
43 J. M. Alía and H. G. M. Edwards, *Vib. Spectrosc.*, 2000, **24**, 185–200.
44 D. Zhang, Y. Wang, Y. Yang, Y. Zhang, Y. Zhao, M. Pan, Y. Sun, S. Chen, X. Liu, J. Wang and Y. NuLi, *Adv. Energy Mater.*, 2023, **13**, 2301795.
45 Y. Du, Y. Chen, S. Tan, J. Chen, X. Huang, L. Cui, J. Long, Z. Wang, X. Yao, B. Shang, G. Huang, X. Zhou, L. Li, J. Wang and F. Pan, *Energy Storage Mater.*, 2023, **62**, 102939.

46 K. Ouyang, D. Ma, N. Zhao, Y. Wang, M. Yang, H. Mi, L. Sun, C. He and P. Zhang, *Adv. Funct. Mater.*, 2021, **32**, 2109749.
47 R. Attias, M. Salama, B. Hirsch, Y. Goffer and D. Aurbach, *Joule*, 2019, **3**, 27–52.
48 Q. Zhao, S. Stalin and L. A. Archer, *Joule*, 2021, **5**, 1119–1142.
49 G. Yang, Y. Li, C. Zhang, J. Wang, Y. Bai, C. Y. J. Lim, M.-F. Ng, Z. Chang, S. Kumar, Z. Sofer, W. Liu and Z. W. Seh, *Nano Lett.*, 2022, **22**, 9138–9146.
50 J. Xiao, X. Zhang, H. Fan, Q. Lin, L. Pan, H. Liu, Y. Su, X. Li, Y. Su, S. Ren, Y. Lin and Y. Zhang, *Adv. Energy Mater.*, 2022, **12**, 2202602.
51 D.-T. Nguyen, A. Y. S. Eng, M.-F. Ng, V. Kumar, Z. Sofer, A. D. Handoko, G. S. Subramanian and Z. W. Seh, *Cell Rep. Phys. Sci.*, 2020, **1**, 100265.
52 Y. Li, G. Yang, C. Zhang, W. Y. Lieu, C. Y. J. Lim, S. Sun, J. Wang, S. Jiang, Z. Xing, Z. Sofer, M.-F. Ng, W. Liu and Z. W. Seh, *Adv. Funct. Mater.*, 2023, **33**, 2210639.
53 X. Fan, L. Chen, X. Ji, T. Deng, S. Hou, J. Chen, J. Zheng, F. Wang, J. Jiang, K. Xu and C. Wang, *Chem*, 2018, **4**, 174–185.
54 H. Dou, X. Zhao, Y. Zhang, W. Zhao, Y. Yan, Z.-F. Ma, X. Wang and X. Yang, *Nano Energy*, 2021, **86**, 106087.
55 O. Mizrahi, N. Amir, E. Pollak, O. Chusid, V. Marks, H. Gottlieb, L. Larush, E. Zinigrad and D. Aurbach, *J. Electrochem. Soc.*, 2008, **155**, A103.
56 J. H. Kwak, Y. Jeoun, S. H. Oh, S. Yu, J.-H. Lim, Y.-E. Sung, S.-H. Yu and H.-D. Lim, *ACS Energy Lett.*, 2022, **7**, 162–170.
57 J. H. Um, S. J. Kim, J. H. Hyun, M. Kim, S. H. Lee and S. H. Yu, *Acc. Chem. Res.*, 2023, **56**, 440–451.
58 Z. Shen, J. Mao, G. Yu, W. Zhang, S. Mao, W. Zhong, H. Cheng, J. Guo, J. Zhang and Y. Lu, *Angew. Chem., Int. Ed.*, 2023, **62**, e202218452.
59 M. D. Levi, E. Lancry, H. Gizbar, Z. Lu, E. Levi, Y. Gofer and D. Aurbach, *J. Electrochem. Soc.*, 2004, **151**, A1044.
60 L. Cui, L. Zhou, K. Zhang, F. Xiong, S. Tan, M. Li, Q. An, Y.-M. Kang and L. Mai, *Nano Energy*, 2019, **65**, 103902.
61 I. A. Rodriguez-Perez, Y. Yuan, C. Bommier, X. Wang, L. Ma, D. P. Leonard, M. M. Lerner, R. G. Carter, T. Wu, P. A. Greaney, J. Lu and X. Ji, *J. Am. Chem. Soc.*, 2017, **139**, 13031–13037.
62 F. Guo, C. Wu, S. Chen, X. Ai, F. Zhong, H. Yang and J. Qian, *ACS Mater. Lett.*, 2020, **2**, 358–366.
63 H. G. Yang, C. H. Sun, S. Z. Qiao, J. Zou, G. Liu, S. C. Smith, H. M. Cheng and G. Q. Lu, *Nature*, 2008, **453**, 638–641.
64 F. Maurer, J. Brötz, S. Karim, M. E. Toimil Molares, C. Trautmann and H. Fuess, *Nanotechnology*, 2007, **18**, 135709.

